# Crust-core properties of neutron stars in the Nambu–Jona-Lasinio model *

Si-Na Wei(韦斯纳) Rong-Yao Yang(杨荣瑶) Wei-Zhou Jiang(蒋维洲)[1)]
School of Physics, Southeast University, Nanjing 211189, China

**Abstract:** We adopt the Nambu–Jona-Lasinio (NJL) model to study the crust-core transition properties in neutron stars (NSs). For a given momentum cutoff and symmetry energy of saturation density in the NJL model, decreasing the slope of the symmetry energy gives rise to an increase in the crust-core transition density and transition pressure. Given the slope of the symmetry energy at saturation density, the transition density and corresponding transition pressure increase with increasing symmetry energy. The increasing trend between the fraction of the crustal moment of inertia and the slope of symmetry energy at saturation density indicates that a relatively large momentum cutoff of the NJL model is preferred. For a momentum cutoff of 500 MeV, the fraction of the crustal moment of inertia clearly increases with the slope of symmetry energy at saturation density. Thus, at the required fraction (7%) of the crustal moment of inertia, the NJL model with momentum cutoff of 500 MeV and a large slope of the symmetry energy of saturation density can give the upper limit of the mass of the Vela pulsar to be above 1.40 $M_{\odot}$.

**Keywords:** neutron stars, Nambu-Jona-Lasinio model, glitches, crust-core transition

**PACS:** 11.30.Rd, 21.65.Jk, 26.60.Dd **DOI:** 10.1088/1674-1137/42/5/054103

## 1 Introduction

Neutron stars (NSs) feature many properties that are dominated by the nuclear equation of state (EOS). For instance, the NS maximum mass depends mainly on the nuclear EOS of isospin symmetric matter at densities in excess of a few times saturation density $\rho_0$, and the NS radius is primarily determined by the slope of the symmetry energy in the density range of 1 to 2 $\rho_0$ [1]. The nuclear EOS also plays a decisive role in the dynamical evolution of the NS, such as pulsar glitches. Historically, pulsar glitches were thought to be the result of starquakes [2]. However, this kind of interpretation cannot explain why the glitches occur about every three years on average. To solve this problem, a corequake model was established [3]. Similarly, the existence of a solid core in the corequake model is also unpersuasive. Nowadays, glitches are though to result from angular momentum transfer between the liquid interior and the solid crust [4–9]. When the crust rotation slows down for the emission of magnetic dipole radiation, the inner crust, where there is a neutron superfluid, rotates more rapidly than the crust because of the absence of viscous drag. Since there is a lag between the crust and the neutron superfluid, a Magnus force is exerted on the superfluid vortices. The superfluid vortices, pinned in the crystal lattice of neutron-rich nuclei of the inner crust, will be unpinned when the lag reaches a critical point, and transfer their angular momentum to the solid crust. This leads to a sudden increase of the pulsar rotation rate, i.e., the glitches. Large glitches of the Vela pulsar suggest that about 1.6 percent of the total moment of inertia resides in the crust of the Vela pulsar [6, 9, 10]. When the crustal entrainment is taken into account, which means the nondissipative elastic scattering of unbound neutrons by the crystal lattice reducing the neutron superfluid, the lower limit of the fraction of crustal moment of inertia needs to increase significantly to 7 percent [9, 11, 12] in order to explain the large glitches of the Vela pulsar. In researching NS glitches, it is very important to study the phase transition from homogeneous matter at higher densities to inhomogeneous matter at low densities. The predicted transition density $\rho_{\rm t}$ and the transition pressure $P_{\rm t}$ are significant for understanding the crust-core properties of NS. In the past, lots of theoretical models were used to understand these low-density transition properties [8, 10, 13–16].

In this paper, we employ the Nambu–Jona-Lasinio (NJL) model, which respects the chiral symmetry to describe the crust-core properties of a NS. The original NJL model, which was built in analogy to the BCS theory, was established on the nucleonic degrees of freedom [17]. The

Received 25 October 2017, Revised 25 February 2018, Published online 20 April 2018

∗ Supported by National Natural Science Foundation of China (11775049, 11275048) and the China Jiangsu Provincial Natural Science Foundation (BK20131286)

1) E-mail: wzjiang@seu.edu.cn

pion in the NJL model was treated as a Goldstone boson of the spontaneously broken chiral symmetry with the nucleon as the elementary fermion. Whereas chiral symmetry is indeed an important symmetry of low-energy QCD, the NJL model has been widely used to describe quark matter [18–20]. Since confinement is absent in the NJL model, the original NJL model with the nucleonic degrees of freedom also remains widely used. It should be noted that the original NJL model cannot reproduce the saturation properties of nuclear matter. The saturation problem of the NJL model was cured by introducing the scalar-vector interaction [21–23]. In our previous work, a good fit was achieved between the NJL parametrizations on the nucleonic level and the available saturation properties and nuclear EOS of pure neutron matter [24]. However, due to the constraints on the nuclear EOS imposed by chiral symmetry, the NJL model has some different characteristics from other models. For instance, the symmetry energy of the NJL model can have the same trends of stiffness at both subsaturation and supranormal densities, in sharp contrast to the usual models, where a soft symmetry energy at higher densities means a stiff symmetry energy at lower densities [24]. The difference is mainly caused by a faster eclipse of nucleon mass due to the partial restoration of chiral symmetry in the medium. With the saturation properties and EOS of pure neutron matter in nice agreement with the available constraints, it is interesting in this work to investigate the properties of NS matter with the NJL model, which may bring some differences in predicting the onset of pulsar glitches [6].

The paper is arranged as follows. In Section 2, the formalism for obtaining the nuclear EOS of asymmetric matter and transition density will be given. The numerical results and discussions are presented in Section 3. Finally, a brief summary is given.

## 2 Formalism

The extended NJL model contains scalar, vector, isovector, scalar-vector and isovector-scalar interactions. The vector-vector and isovector-vector interactions are not considered, because the vector-vector interaction may lead to the pressure exceeding the energy density, depending on the sign of the coupling strength, and the isovector-vector interaction may produce a negative symmetry energy which will render the NS unstable [24]. The Lagrangian of the extended NJL model can be written as [21–26]:

$$\begin{aligned}\mathcal{L} =\ & \bar{\psi}(i\gamma_\mu\partial^\mu-m_0)\psi+\frac{G_{\rm S}}{2}[(\bar{\psi}\psi)^2-(\bar{\psi}\gamma_5\tau\psi)^2]\\ &-\frac{G_{\rm V}}{2}[(\bar{\psi}\gamma_\mu\psi)^2+(\bar{\psi}\gamma_\mu\gamma_5\psi)^2]\\ &+\frac{G_\rho}{2}[(\bar{\psi}\gamma_\mu\tau\psi)^2+(\bar{\psi}\gamma_\mu\gamma_5\tau\psi)^2]\\ &+\frac{G_{\rm SV}}{2}[(\bar{\psi}\psi)^2-(\bar{\psi}\gamma_5\tau\psi)^2]\\ &\cdot[(\bar{\psi}\gamma_\mu\psi)^2+(\bar{\psi}\gamma_\mu\gamma_5\psi)^2]\\ &+\frac{G_{\rho{\rm S}}}{2}[(\bar{\psi}\gamma_\mu\tau\psi)^2+(\bar{\psi}\gamma_\mu\gamma_5\tau\psi)^2]\cdot\\ &[(\bar{\psi}\psi)^2-(\bar{\psi}\gamma_5\tau\psi)^2],\end{aligned}\tag{1}$$

where $m_0$ is the bare nucleon mass. $G_{\rm S}$, $G_{\rm V}$, $G_\rho$, $G_{\rm SV}$ and $G_{\rho{\rm S}}$ are the scalar, vector, isovector, scalar-vector and isovector-scalar coupling constants, respectively. It is easy to see that the Lagrangian is chiral symmetric when $m_0$=0.

In the mean field approximation, the Lagrangian can be simplified to:

$$\begin{aligned}\mathcal{L} =\ & \mathcal{L}_0+\mathcal{L}_{IV}=\bar{\psi}[i\gamma_\mu\partial^\mu-m(\rho,\rho_{\rm S})\\ &-\gamma^0\Sigma(\rho,\rho_{\rm S},\rho_3)]\psi-U(\rho,\rho_{\rm S},\rho_3),\end{aligned}\tag{2}$$

where $m$, $\Sigma$ and $U$ are defined as

$$m(\rho,\rho_{\rm S}) = m_0-(G_{\rm S}+G_{\rm SV}\rho^2+G_{\rho{\rm S}}\rho_3^2)\rho_{\rm S},\tag{3}$$

$$\begin{aligned}\Sigma(\rho,\rho_{\rm S},\rho_3) =\ & G_{\rm V}\rho+G_\rho\rho_3\tau_3-G_{\rm SV}\rho_S^2\rho\\ &-G_{\rho{\rm S}}\rho_3\rho_{\rm S}^2\tau_3,\end{aligned}\tag{4}$$

$$\begin{aligned}U(\rho,\rho_{\rm S},\rho_3) =\ & \frac{1}{2}(G_{\rm S}\rho_S^2-G_{\rm V}\rho^2-G_\rho\rho_3^2+3G_{\rm SV}\rho_S^2\rho^2\\ &+3G_{\rho{\rm S}}\rho_3^2\rho_{\rm S}^2).\end{aligned}\tag{5}$$

Equation (3) is the gap equation for the nucleon effective mass in this NJL model. Here $\rho=<\bar{\psi}\gamma^0\psi>$, $\rho_3=<\bar{\psi}\gamma^0\tau_3\psi>$ and $\rho_{\rm S}=<\bar{\psi}\psi>$ are the vector, isovector and scalar densities, respectively,

$$\rho = \sum_{\rm i=p,n}\nu_{\rm i}\int_0^{p_{F_{\rm i}}}\frac{{\rm d}^3p}{(2\pi)^3},\ \rho_3=\rho_{\rm p}-\rho_{\rm n},\tag{6}$$

$$\rho_{\rm S} = -\sum_{\rm i=p,n}\nu_{\rm i}\int_{p_{F_{\rm i}}}^{\Lambda}\frac{{\rm d}^3p}{(2\pi)^3}\frac{m}{\sqrt{p^2+m^2}},\tag{7}$$

where $\nu_{\rm i}$ is the spin degeneracy, and $\Lambda$ is the momentum cutoff. From the above Lagrangian, we may obtain the energy density

$$\begin{aligned}\epsilon =\ & -\sum_{\rm i=p,n}\nu_{\rm i}\int_{p_{F_{\rm i}}}^{\Lambda}\frac{{\rm d}^3p}{(2\pi)^3}(p^2+m^2)^{1/2}+\frac{G_{\rm V}\rho^2}{2}\\ &+\frac{G_\rho\rho_3^2}{2}+\frac{G_{\rm S}\rho_{\rm S}^2}{2}+\frac{G_{\rm SV}\rho^2\rho_{\rm S}^2}{2}\\ &+\frac{G_{\rho{\rm S}}{\rho_3}^2\rho_{\rm S}^2}{2}+\epsilon_0,\end{aligned}\tag{8}$$

where the $\epsilon_0$ is introduced to give the vanishing energy density of the vacuum state [21]. The pressure can be obtained from the thermodynamic relation

$$P=\sum_{\rm i=p,n}\mu_{\rm i}\rho_{\rm i}-\epsilon,\mu_{\rm i}=\frac{\partial\epsilon}{\partial\rho_{\rm i}},\tag{9}$$

and it is given explicitly as

$$P = -\sum_{\rm i=p,n}\frac{\nu_{\rm i}}{3}\int_{p_{F_{\rm i}}}^{\Lambda}\frac{{\rm d}^3k}{(2\pi)^3}\frac{k^2}{\sqrt{k^2+m^2}}+\frac{G_{\rm V}\rho^2}{2} +\frac{G_\rho\rho_3^2}{2}-\frac{G_{\rm S}\rho_{\rm S}^2}{2}-\frac{3G_{\rm SV}\rho_{\rm S}^2\rho^2}{2} -\frac{3G_{\rho{\rm S}}{\rho_3}^2\rho_{\rm S}^2}{2}-\frac{2\Lambda^3\sqrt{\Lambda^2+m^2}}{3\pi^2}-\epsilon_0. \quad (10)$$

From the energy density, we can derive the symmetry energy as

$$E_{\rm sym}(\rho)=\frac{1}{2}\frac{\partial^2(\epsilon/\rho)}{\partial\delta^2}\bigg|_{\delta=0}=\frac{p_{\rm F}^2}{6E_{\rm F}}+\frac{1}{2}G_\rho\rho-\frac{1}{2}G_{\rho{\rm S}}\rho_{\rm S}^2\rho, \quad (11)$$

where $\delta=(\rho_{\rm n}-\rho_{\rm p})/\rho$ is the isospin asymmetry parameter and $E_{\rm F}=\sqrt{p_{\rm F}^2+m^2}$. The slope of the symmetry energy at saturation density is defined as

$$L=3\rho_0\frac{\partial E_{\rm sym}}{\partial\rho}\bigg|_{\rho_0}. \quad (12)$$

In this work, we consider the simplest composition for NS matter: neutrons, protons and electrons. The NS composition can be obtained from solving the gap equation (Eq. (3)) and the conditions of chemical equilibrium and charge neutrality.

$$\mu_{\rm n}=\mu_{\rm p}+\mu_{\rm e},\quad \rho_{\rm p}=\rho_{\rm e}. \quad (13)$$

The thermodynamical stability condition will lead to the constraints for pressure and chemical potential [8, 27, 28].

$$-\left(\frac{\partial(P+P_{\rm e})}{\partial v}\right)_\mu>0, \quad (14)$$

$$-\left(\frac{\partial\mu}{\partial q_{\rm c}}\right)_v>0, \quad (15)$$

where $P_{\rm e}$ is the pressure of electrons, $v=1/\rho$ is the volume per baryon and $q_{\rm c}=(\rho_{\rm p}-\rho_{\rm e})/\rho$ is the charge fraction. Equation (15) is usually valid. Since $P_{\rm e}$ is only a function of the chemical potential, Eq. (14) can be simplified as

$$-\left(\frac{\partial P}{\partial v}\right)_\mu>0. \quad (16)$$

The above constraint leads to the following inequality [8, 13, 14, 27, 28]:

$$V = \rho^2\frac{\partial^2E(\rho,\delta)}{\partial\rho^2}+2\rho\frac{\partial E(\rho,\delta)}{\partial\rho} -\left(2\rho\frac{\partial^2E(\rho,\delta)}{\partial\rho\partial\delta}\right)^2\left(\frac{4\partial^2E(\rho,\delta)}{\partial\delta^2}\right)^{-1}>0. \quad (17)$$

The crust-core transition density $\rho_{\rm t}$ can be obtained by solving the coupled equations $V=0$ and Eq. (13). The corresponding crust-core transition pressure can thus be obtained by the following equation [8, 14]:

$$P_{\rm t} = \frac{\kappa}{9}\frac{\rho_{\rm t}^2}{\rho_0}\left(\frac{\rho_{\rm t}}{\rho_0}-1\right)+\rho_{\rm t}\delta_{\rm t}\left[\frac{1-\delta_{\rm t}}{2}E_{\rm sym}(\rho_{\rm t}) +\left(\rho\frac{{\rm d}E_{\rm sym}(\rho)}{{\rm d}\rho}\right)_{\rho_{\rm t}}\delta_{\rm t}\right], \quad (18)$$

where $\kappa$ is the incompressibility of symmetry nuclear matter at saturation density $\rho_0$.

## 3 Results and discussions

The momentum cutoffs are chosen as 320, 350, 400 and 500 MeV, according to the saturation properties, especially the incompressibility. The parameters, listed in Table 1, can be obtained as follows. With the chosen momentum cutoff, the scalar density of the vacuum state $\rho_{\rm S}^{\rm vac}$ can be obtained. The bare nucleon mass $m_0$ can be solved by using $\rho_{\rm S}^{\rm vac}$ and the Gell-Mann-Oakes-Renner (GMOR) relation of nucleons $m_\pi^2f_\pi^2=m_0\rho_{\rm S}^{\rm vac}$ ($m_\pi=140$ MeV, $f_\pi=93$ MeV) [18, 22]. In so doing, we obtain a small bare nucleon mass $m_0$ that interprets the consistency with the understanding that the mass acquisition arises dominantly from the non-perturbative vacuum. This is consistent with the conclusion in Ref. [29] that the nucleon mass coming from an explicit chiral symmetry breaking should not be larger than 160 MeV. Yet, we note that there are various considerations to make the choice of the bare nucleon mass [26, 30]. For instance, a different parametrization with very large bare mass was considered in a similar model [26]. We then determine $G_{\rm S}$ through the gap equation (Eq. (3)) in the vacuum state. $G_{\rm SV}$ and $G_{\rm V}$ are obtained by satisfying the saturation property, namely, the energy per nucleon $\epsilon/\rho-M_{\rm N}=-16$ MeV ($M_{\rm N}=938$ MeV) at $\rho_0=0.160$ fm$^{-3}$. The choices of the isovector coupling constant $G_\rho$ and isovector-scalar coupling constant $G_{\rho{\rm S}}$ in Table 2 are constrained by properties of symmetry energy at saturation density.

To provide a convincing study, we restrict the EOS to be consistent with the KaoS experiment [31–34] and the collective flow data in heavy-ion collisions [35]. As shown in Fig. 1, the pressure of the NJL model with the momentum cutoff of 320 and 350 MeV surpasses the constraints extracted from both the KaoS experiment and the collective flow data. We see that the pressure with the momentum cutoff of 400 MeV can satisfy the KaoS experiment well and the one with 500 MeV is very close to the constraint from the KaoS experiment. Besides, the pressure with the momentum cutoff of 500 MeV can pass through the constraints extracted from the collective flow data in the full density region, while the one with the momentum cutoff of 400 MeV will surpass the collective flow data constraint beyond $3\rho_0$ because its critical density, which is determined as $p_{\rm F}=\Lambda$, is much smaller than

Table 1. The NJL parameter sets with various cutoffs that are adjusted at saturation density $\rho_0=0.16\text{fm}^{-3}$. $\rho_c$, evaluated by the relation $p_F=\Lambda$, is the critical density for chiral symmetry restoration.

| $\Lambda$/MeV | $G_S/(\text{GeV}\cdot\text{fm}^3)$ | $m_0$/MeV | $G_{SV}/(\text{GeV}\cdot\text{fm}^9)$ | $G_V/(\text{GeV}\cdot\text{fm}^3)$ | $\kappa$/MeV | $\rho_c/\rho_0$ |
|---|---|---|---|---|---|---|
| 320 | 3.067 | 79.2 | 4.553 | 2.736 | 318 | 1.81 |
| 350 | 2.409 | 60.9 | 3.482 | 2.173 | 262 | 2.37 |
| 400 | 1.669 | 41.3 | 2.054 | 1.581 | 296 | 3.53 |
| 500 | 0.896 | 21.7 | 0.879 | 1.156 | 315 | 6.90 |

that with the momentum cutoff of 500 MeV. It should be noted that the marginal consistency with the available constraints at high densities is due to the model's chiral character, which is not considered in the transport models that are used to extract those constraints. The nice agreement with the available constraints at lower densities demonstrates that it is meaningful to use the EOS with the momentum cutoff of 400 and 500 MeV to study the NS crust-core transitional properties at low densities. We also depict the pressure with the relativistic mean-field (RMF) models NL3 [36], NL-SH [37] and TM1 [38] for comparison. The pressure with NL3 and NL-SH surpasses the constraints from both the KaoS experiment and the collective flow data. However, the pressure with TM1 passes through constraints from both the KaoS experiment and the collective flow data. As we can see from Fig. 1, the NJL pressure with the momentum cutoff of 400 and 500 MeV is between the pressure with NL3 (NL-SH) and the pressure with TM1. In the following, we perform the investigation with momentum cutoffs of 400 and 500 MeV.

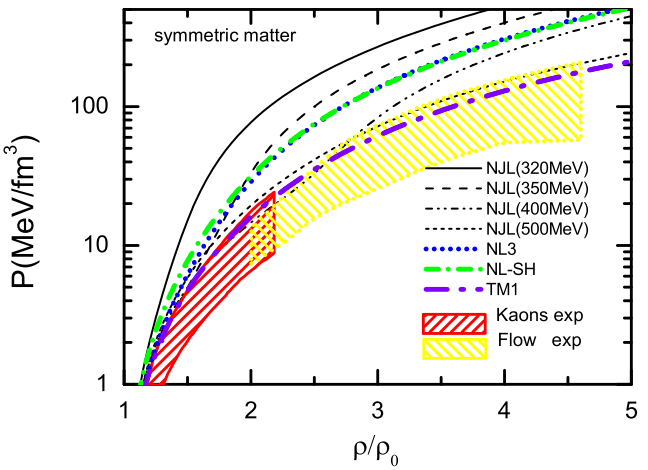


Fig. 1. (color online) The pressure as a function of density for symmetric nuclear matter. The red region represents the constraints from the KaoS experiment [31–34] and the yellow region the constraints from the collective flow data [35]. The pressure with the RMF models NL3, NL-SH and TM1 are also depicted for comparison.

The symmetry energy at saturation density extracted from terrestrial nuclear experiments and astrophysical observations is around $E_{sym}(\rho_0)\sim 26-35.8$ MeV at saturation density [39–47]. The slope of the symmetry energy at saturation density still has large uncertainties, ranging from 19 to 110 MeV in analyses of terrestrial nuclear experiments [40–42, 48–50], or from 43 to 130 MeV in analyses of astrophysical observations [47, 51–54]. In fact, the uncertainty of the slope of the symmetry energy may grow with increasing symmetry energy at saturation density. For instance, the slope of saturation density may change from 60 to 110 at $E_{sym}(\rho_0)=35.0$ MeV [43, 44]. Even though the average slope of symmetry energy of 40–60 MeV is extracted according to the observational/experimental data [39, 41, 44–46, 54], a value beyond this average domain cannot be excluded, especially when the larger symmetry energy is considered. In this study, the slope of the symmetry energy at saturation density is thus not just limited to the average domain, though we are actually in reference to this average domain. As listed in Table 2, the symmetry energy at saturation density is chosen as an average value $E_{sym}(\rho_0)=31.6$ MeV [39] and a comparatively larger value $E_{sym}(\rho_0)=35.0$ MeV. The slopes of symmetry energy of saturation density with $\Lambda=400$ MeV are chosen as 50.0, 93.6 and 108.7 MeV. The slopes of symmetry energy of saturation density with $\Lambda=500$ MeV and $E_{sym}(\rho_0)=31.6$ MeV are chosen as 64.0, 85.6 and 108.6 MeV, and those with $\Lambda=500$ MeV and $E_{sym}(\rho_0)=35.0$ MeV are chosen as 70.0, 85.6 and 108.6 MeV. The slopes of symmetry energy of different momentum cutoffs at saturation density are correspondingly locating in the domain of analyses of terrestrial nuclear experiments/astrophysical observations $L(\rho_0)\sim$ 19–130 MeV. The minimum slopes of the symmetry energy of saturation density at $E_{sym}(\rho_0)=35.0$ MeV and 31.6 MeV are different with $\Lambda=500$ MeV, whereas they are chosen to be the same with $\Lambda=400$ MeV. As the chiral symmetry is restored at high densities, the contribution from the isovector-scalar term is very close to zero, and the isovector term dominates the symmetry energy. The symmetry energy is very different at high density when the isovector-scalar coupling constant is taken to be zero, because of the nonvanishing isovector coupling constant. However, the symmetry energy is very close at high densities when the isovector coupling constant equals zero for minor contribution from the isovector-scalar term. For example, with $\Lambda=400$ MeV, the curves with the same

Table 2. The crust-core transition density $\rho_t$ and transition pressure $P_t$ with respect to the slope of the symmetry energy $L(\rho_0)$ at saturation density with $\Lambda = 400$ and 500 MeV. The coupling constants $G_\rho$ and $G_{\rho S}$ are set by fitting $E_{sym}(\rho_0)$=31.6 MeV or 35.0 MeV at saturation density. $\kappa$ is the incompressibility at saturation density $\rho_0$. For comparison, the transition properties of the RMF models NL3, NL-SH and TM1 are also presented.

| $\Lambda$/MeV | $\rho_0$/fm$^{-3}$ | $\kappa$/MeV | $L(\rho_0)$/MeV | $E_{sym}(\rho_0)$/MeV | $\rho_t$/fm$^{-3}$ | $P_t$/(MeV·fm$^{-3}$) | $G_\rho$/(GeV·fm$^3$) | $G_{\rho S}$/(GeV·fm$^9$) |
|---|---|---|---|---|---|---|---|---|
| 400 | | | 50.0 | 31.6 | 0.088 | 0.480 | 0.011 | -1.405 |
| 400 | | | 93.6 | 31.6 | 0.077 | 0.403 | 0.193 | 0 |
| 400 | 0.160 | 296 | 108.7 | 31.6 | 0.069 | 0.306 | 0.256 | 0.485 |
| 400 | | | 50.0 | 35.0 | 0.090 | 0.604 | 0.011 | -1.734 |
| 400 | | | 93.6 | 35.0 | 0.081 | 0.577 | 0.193 | -0.329 |
| 400 | | | 108.7 | 35.0 | 0.077 | 0.523 | 0.256 | 0.154 |
| 500 | | | 64.0 | 31.6 | 0.095 | 0.636 | 0.012 | -0.299 |
| 500 | | | 85.6 | 31.6 | 0.085 | 0.507 | 0.223 | 0 |
| 500 | 0.160 | 315 | 108.6 | 31.6 | 0.079 | 0.412 | 0.446 | 0.316 |
| 500 | | | 70.0 | 35.0 | 0.096 | 0.767 | 0.014 | -0.357 |
| 500 | | | 85.6 | 35.0 | 0.090 | 0.707 | 0.166 | -0.141 |
| 500 | | | 108.6 | 35.0 | 0.082 | 0.592 | 0.389 | 0.175 |
| NL3 | 0.148 | 271 | 118.4 | 37.3 | 0.065 | 0.461 | | |
| NS-SH | 0.146 | 357 | 113.7 | 36.1 | 0.074 | 0.456 | | |
| TM1 | 0.145 | 279 | 110.5 | 36.8 | 0.071 | 0.568 | | |

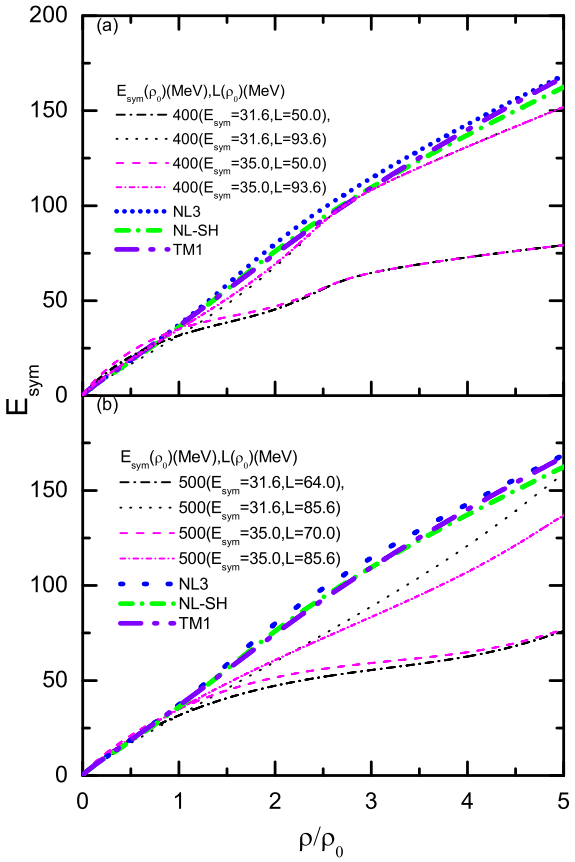


Fig. 2. (color online) The symmetry energy as a function of density. The corresponding isovector coupling constant ($G_\rho$) is given in Table 2. For comparison, the results with the RMF models NL3, NL-SH and TM1 are also displayed.

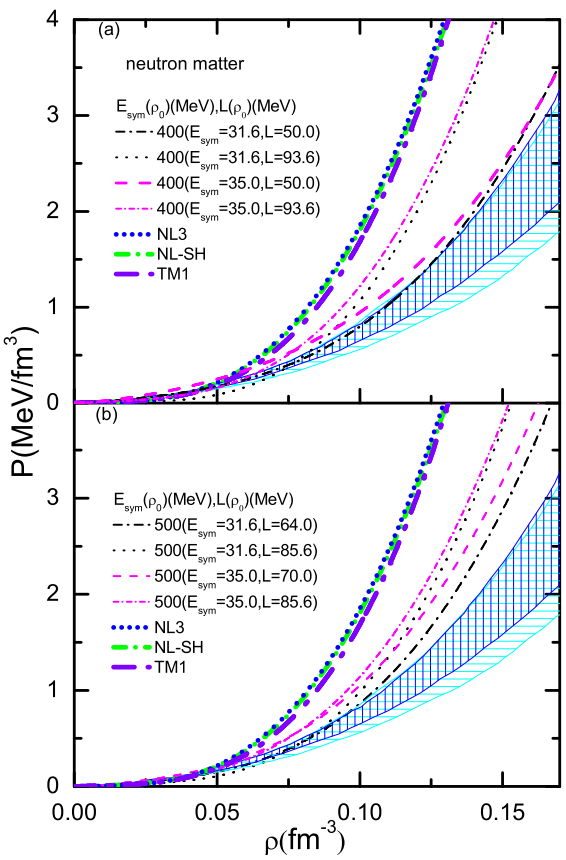


Fig. 3. (color online) The pressure as a function of density for neutron matter. The blue area is the quantum Monte Carlo result [55], and the cyan area is the microscopic result based on chiral NN and 3N interactions [56].

slope but different symmetry energies at saturation density nearly overlap at high densities, as shown in Fig. 2.

Besides the constraints on symmetric matter properties and the symmetry energy at saturation density, we make a more comprehensive comparison with quantum Monte Carlo results [55] and microscopic calculations based on chiral NN and 3N interactions [55], that mainly concern the behavior of the symmetry energy below saturation density. As can be seen from Fig. 3, the pressure of neutron matter with a relatively small slope in the NJL model ($L(\rho_0)$=50 MeV with $\Lambda$=400 MeV and $L(\rho_0)$=64 MeV with $\Lambda$=500 MeV) marginally satisfies the ab-initio constraints at sub-saturation densities. When the slope of symmetry energy is relatively large, the pressure of neutron matter is just close to the constraints below 0.1 fm$^{-3}$. Note that the ab-initio constraints from Refs. [55] and [56] produced a relatively small slope of symmetry energy. Generally, our results agree with the ab-initio constraints, though the deviation from the ab-initio constraints becomes large for the use of the large slope parameter of the symmetry energy in the NJL model.

The crust-core transition density $\rho_t$ is obtained by solving the coupled equations Eq. (17) and Eq. (13), and the corresponding transition pressure $P_t$ is obtained by solving Eq. (18). The crust-core transition density $\rho_t$ generally increases with decreasing slope of the symmetry energy at saturation density [14–16]. However, the dependence of the transition pressure on the slope of the symmetry energy at saturation density is model-dependent [16]. A momentum-dependent interaction (MDI) model shows that the transition pressure decreases with increasing slope of the symmetry energy at saturation density[14], whereas the relativistic nuclear energy density functionals support that the transition pressure increases with increasing slope of the symmetry energy [15]. In the NJL model, we find that the transition pressure decreases with increasing slope of the symmetry energy at saturation density. For instance, with $E_{\rm sym}(\rho_0)$=31.6 MeV and $\Lambda$=400 MeV, as the slope of the symmetry energy at saturation density increases from 50.0 to 93.6 MeV, the transition density decreases from 0.088 to 0.077 fm$^{-3}$, and the corresponding pressure decreases from 0.480 to 0.403 MeV·fm$^{-3}$. We also study the increasing trend between crust-core transition properties and the symmetry energy at saturation density. When the slope of the symmetry energy at saturation density is fixed, we find that the transition density and the corresponding transition pressure increase with increasing symmetry energy. For instance, when the slope of the symmetry energy of $\Lambda$=400 MeV at saturation density is set to be 93.6 MeV, the transition density increases from 0.077 fm$^{-3}$ to 0.088 fm$^{-3}$ when the symmetry energy increases from $E_{\rm sym}(\rho_0) = 31.6$ MeV to $E_{\rm sym}(\rho_0) = 35.0$ MeV, and the corresponding pressure increases from 0.403 MeV·fm$^{-3}$ to 0.577 MeV·fm$^{-3}$. In short, the crust-core transition properties depend not only on the slope of symmetry energy but also on the symmetry energy at saturation density [16, 40].

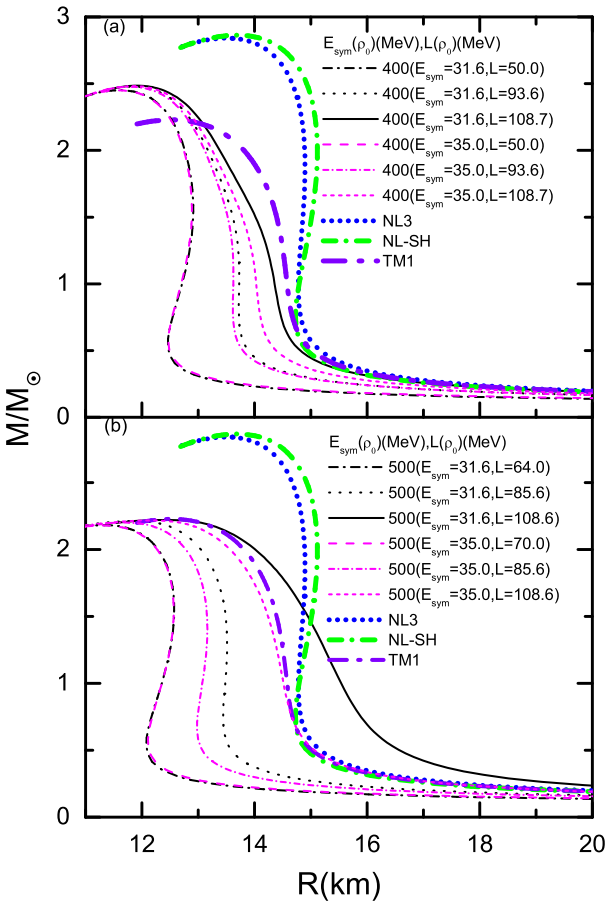


Fig. 4. (color online) Mass versus radius for the cutoffs of 400 and 500 MeV of neutron star mass. For comparison, the results with the RMF models are also displayed.

With the crust-core transition properties and EOS of NS matter, the radius-mass relations can be obtained by solving the standard Tolman-Oppenheimer-Volkoff (TOV) [57, 58] equation. We adopt the EOS obtained in this work at densities above the transition density, while we employ the standard low-density EOS [59, 60] below the transition density where it is an inhomogeneous phase. As the NS central density may exceed the critical density $\rho_c$ for $\Lambda$=400 MeV [24], one needs to check the validity of NJL model with $\Lambda$=400 MeV above $\rho_c$. As the density increases continuously, the Fermi momentum increases to be close to the cutoff, resulting in the restoration of chiral symmetry. When the Fermi momentum exceeds the cutoff, we find that fortunately the nucleon effective mass $m$ and the scalar density $\rho_S$ change continuously with the density and are very close to zero.

Table 3. Some main NS properties of Fig. 4 and Fig. 5 obtained with the parametrizations of Table 2. $M_{\rm max}$ is the NS maximum mass, and $\rho_{\rm cen}$ is the NS central density. The radius R is in units of km. $\Delta I/I$, the fraction of the crustal moment of inertia, is defined in Eq. (19).

| $\Lambda$/MeV | $L(\rho_0)$/MeV | $E_{\rm sym}(\rho_0)$/MeV | ($M_{\rm max}/M_\odot$, $R$, $\rho_{\rm cen}/\rho_0$) | $R(1.4M_\odot)$ | $M/M_\odot(\Delta I/I$=0.07) |
|---|---|---|---|---|---|
| 400 | 50.0 | 31.6 | (2.45, 11.6, 5.45) | 12.9 | 1.12 |
| 400 | 93.6 | 31.6 | (2.48, 11.8, 5.65) | 13.7 | 1.20 |
| 400 | 108.7 | 31.6 | (2.48, 11.9, 5.50) | 14.0 | 1.12 |
| 400 | 50.0 | 35.0 | (2.45, 11.6, 5.30) | 12.9 | 1.26 |
| 400 | 93.6 | 35.0 | (2.48, 11.8, 5.30) | 13.6 | 1.37 |
| 400 | 108.7 | 35.0 | (2.48, 11.8, 5.65) | 13.9 | 1.37 |
| 500 | 64.0 | 31.6 | (2.18, 11.3, 6.15) | 12.6 | 1.21 |
| 500 | 85.6 | 31.6 | (2.21, 11.8, 6.00) | 13.5 | 1.29 |
| 500 | 108.6 | 31.6 | (2.23, 12.5, 5.60) | 14.9 | 1.47 |
| 500 | 70.0 | 35.0 | (2.18, 11.3, 6.15) | 12.5 | 1.30 |
| 500 | 85.6 | 35.0 | (2.20, 11.7, 5.95) | 13.2 | 1.40 |
| 500 | 108.6 | 35.0 | (2.22, 12.1, 5.80) | 14.3 | 1.53 |
| NL3 | 118.4 | 37.3 | (2.84, 13.5, 4.53) | 14.8 | 1.43 |
| NS-SH | 113.7 | 36.1 | (2.86, 13.7, 4.49) | 15.0 | 1.48 |
| TM1 | 110.5 | 36.8 | (2.23, 12.5, 6.08) | 14.4 | 1.48 |

Thus, no anomalous contributions to the EOS arise from the large Fermi momentum after chiral symmetry restoration, and the model should be valid in the core of neutron stars. As shown in Fig. 4 and Table 3, the NS maximum mass with various momentum cutoffs can easily surpass the lower limit of NS maximum mass, which is about $2M_\odot$ [61, 62], and the NS radius of $1.4M_\odot$ lies in a reasonable domain, which is roughly 10-15 km [63–73]. The mass and radius relations are very important in studying pulsar glitches. The large glitches of the Vela pulsar suggest that about 1.6 percent of the total moment of inertia resides in the crust [9, 10]. When the effects of pairing are small, the neutron superfluid of the inner crust of the NS is still strongly scattering off nuclei due to non-dissipative entrainment effects [12], leading to the decrease of the neutron superfluid density. The fraction of the crustal moment of inertia needs to increase significantly to 7 percent [9, 11] to explain the large glitches of the Vela pulsar. However, the Bragg scattering between the neutron superfluid and nuclei is going to be suppressed when the pairing gap is of the same order as or greater than the strength of the lattice potential [74]. In this case, the required fraction of the crustal moment of inertia may thus be less than 7 percent. In this paper, we just pay attention to the consequences of entrainment under the small pairing effect. In the theoretical calculations, the fraction of the crustal moment of inertia $\Delta I/I$ can be simplified as [75]:

$$\frac{\Delta I}{I} \simeq \frac{28\pi P_{\rm t} R^3}{3Mc^2}\frac{(1-1.67\beta-0.6\beta^2)}{\beta} \times\left[1+\frac{2P_{\rm t}(1+5\beta-14\beta^2)}{\rho_{\rm t} m_{\rm N} c^2\beta^2}\right]^{-1}, \quad (19)$$

where $\Delta I$ is the crustal moment of inertia, $I$ is the total moment of inertia, $\beta=GM/Rc^2$ is the compactness parameter, and $M$ and $R$ are the NS mass and radius, respectively. Given the crust-core transition properties and radius-mass trajectory, the fraction of the crustal moment of inertia can be obtained. As we can see from Eq. (19), the fraction of crustal moment of inertia mainly depends on the radius-mass trajectory and the crust-core transition pressure $P_{\rm t}$. With the fixed momentum cutoff and slope of the symmetry energy at saturation density, the fraction of crustal moment of inertia mainly depends on the crust-core transition pressure $P_{\rm t}$, since the radius-mass trajectories are similar. For instance, with $\Lambda$=400 MeV and $L(\rho_0)$=50 MeV, the fraction of crustal moment of inertia with $E_{\rm sym}(\rho_0)=35.0$ MeV is larger than that with $E_{\rm sym}(\rho_0)=31.6$ MeV, in that the $P_{\rm t}$ of $E_{\rm sym}(\rho_0)=35.0$ MeV is larger. Given the momentum cutoff and symmetry energy at saturation density, since radius-mass trajectory and the crust-core transition pressure $P_{\rm t}$ are different by varying the slope of symmetry energy, the fraction of the crustal moment of inertia depends both on the crust-core transition pressure and on the radius-mass trajectory. As shown in Fig. 5, with $\Lambda$=400 MeV and fixed symmetry energy at saturation density, as the slope of the symmetry energy increases, the fraction of crustal moment of inertia does not increase enough with increasing NS radius to eliminate the reduction of the fraction of crustal moment of inertia caused by the reduction of the crust-core transition pressure. As a result, the fraction of the crustal moment of inertia with $\Lambda$=400 MeV does not increase with increasing slope of symmetry energy at saturation density. However, with $\Lambda$=500 MeV, as the slope of the symmetry energy at saturation density increases, the increase of fraction of crustal moment of inertia caused by increasing the NS radius is larger than the reduction of fraction of

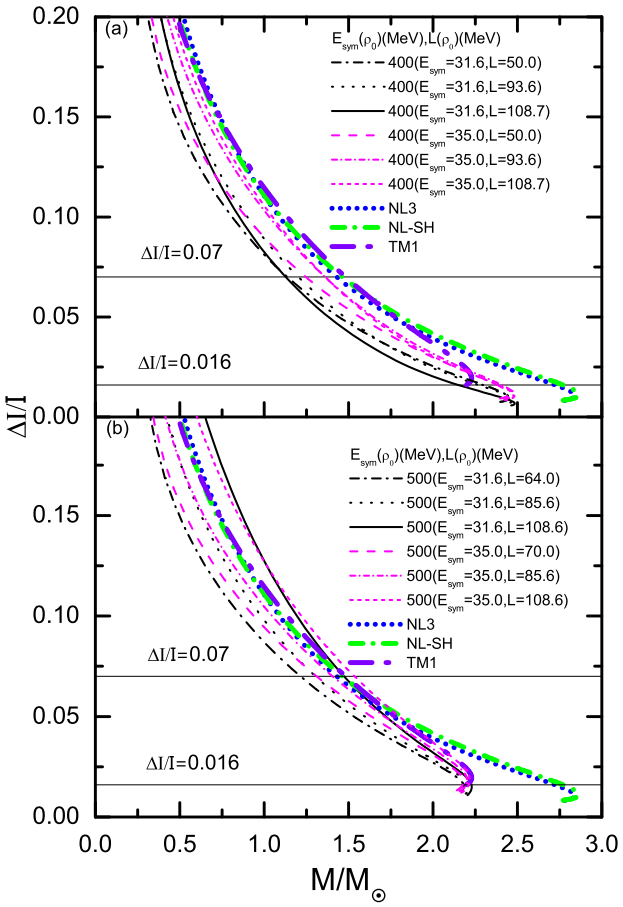


Fig. 5. (color online) Fraction of crustal moment of inertia as a function of neutron star mass. For comparison, the results with the RMF models are also displayed.

crustal moment of inertia caused by the reduction of the crust-core transition pressure. As a consequence, the fraction of the crustal moment of inertia with $\Lambda$=500 MeV increases with increasing slope of symmetry energy at saturation density. Since the NS radius with the larger momentum cutoff increases more sharply than that with small momentum cutoff with increasing slope of symmetry energy at saturation density, the resulting functional between the fraction of the crustal moment of inertia and the slope of symmetry energy at saturation density is dependent on the momentum cutoff. At the required fraction (7%) of the crustal moment of inertia, the parametrization with $\Lambda$=400 MeV cannot give the upper limit of the mass of the Vela pulsar to be above 1.40 $M_\odot$. However, the parametrization with $\Lambda$=500 MeV, where the fraction of the crustal moment of inertia increases with increasing slope of symmetry energy at saturation density, is able to yield the mass of the Vela pulsar above 1.4 $M_\odot$ with a reasonably large slope of the symmetry energy at saturation density. For example, with $\Lambda$=500 MeV, the upper limit of the mass of the Vela pulsar at the necessary fraction (7%) of crustal moment of inertia is 1.47$M_\odot$ for $E_{\rm sym}(\rho_0)$=31.6 MeV and $L(\rho_0)$=108.6 MeV, which is close to the value predicted by the RMF model $NL3_{\rm max}$ [10]. In addition, the parametrization with $\Lambda$=500 MeV and $E_{\rm sym}(\rho_0)$=35.0 MeV yields the upper mass limit of the Vela pulsar as 1.40 and 1.53 $M_\odot$ for $L(\rho_0)$=85.6 and 108.6 MeV, respectively. Since a mass of 1.4 $M_\odot$ can fit the X-ray spectrum of the Vela pulsar well [76], the results with the $\Lambda$=500 MeV parametrization indicate that the crust may carry enough angular momentum to explain the giant frequency glitches of the Vela pulsar.

## 4 Summary

In this work, the NJL model, which has saturation properties on the hadronic level, is used to study the crust-core transition properties in NSs. We have chosen the momentum cutoffs to meet the constraints on the EOS that are extracted from the KaoS experiment and the flow data. It is found that the pressure of the NJL model with the cutoff $\Lambda$ =400 MeV can meet the constraints from the KaoS experiment and the pressure with 500 MeV can satisfy the constraints from the flow data. With the given momentum cutoff and symmetry energy at saturation density, the transition density and corresponding transition pressure increase with decreasing slope of symmetry energy. Besides, with the given momentum cutoff and the slope of symmetry energy at saturation density, the transition density and corresponding transition pressure increase with increasing symmetry energy. At the fraction (7%) of the crustal moment of inertia required by the crustal entrainment, the parametrization with $\Lambda$=400 MeV of the NJL model cannot give the upper limit of the mass of the Vela pulsar above 1.40 $M_\odot$. However, the parametrization with $\Lambda$=500 MeV can yield the mass of Vela pulsar to be above 1.4 $M_\odot$ with the allowed larger values of the symmetry energy and its slope at saturation density. This implies that the crustal angular momentum in the NJL model with reasonable parametrizations can explain the large glitches of the Vela pulsar.

## References


1 J. M. Lattimer, M. Prakash, Astrophys. J., **550**: 426 (2001)
2 M. Ruderman, Nature, **223**: 597 (1969)
3 D. Pines, J. Shaham, M. Ruderman, Nat. Phys. Sci., **237**: 83 (1972)
4 P. W. Anderson and N. Itoh, Nature (London), **256**: 25 (1975)
5 D. Pines, M. Alpar, Nature, **316**: 27 (1985)
6 B. Link, R. I. Epstein, and J. M. Lattimer, Phys. Rev. Lett., **83**: 3362 (1999)
7 J. M. Lattimer, M. Prakash, Science, **304**: 536 (2004)
8 J. M. Lattimer, M. Prakash, Phys. Rep., **442**: 109 (2007)
9 N. Chamel, Phys. Rev. Lett., **110**: 011101 (2013)
10 J. Piekarewicz, F. J. Fattoyev, C. J. Horowitz, Phys. Rev.C, **90**: 015803 (2014)
11 N. Andersson, K. Glampedakis, W. C. G. Ho, and C. M. Espinoza, Phys. Rev. Lett., **109**: 241103 (2012)
12 N. Chamel, Phys. Rev. C, **85**: 035801 (2012)
13 M. Bigdeli and S. Elyasi, Eur. Phys. J. A, **51**(3): 38 (2015)
14 J. Xu, L. W. Chen, B. A. Li, and H. R. Ma, Astrophys. J., **697**: 1549-1568 (2009)
15 Ch. C. Moustakidis et al, Phys. Rev. C, **81**: 065803 (2010)
16 C. Ducoin et al, Phys. Rev. C, **83**: 045810 (2011)
17 Y. Nambu, G. J. Lasinio, Phys. Rev., **122**: 345 (1961)
18 U. Vogl and W. Weise, Prog. Part. Nucl. Phys., **27**: 195-272 (1991)
19 N. D. Merrnin, Rev. Mod. Phys., **64**: 3-49 (1992); Rev. Mod. Phys., **64**: 1163-1163 (1992); Rev. Mod. Phys., **64**: 635-635 (1992); Rev. Mod. Phys., **66**: 249-249 (1994)
20 M. Buballa, Phys. Rept., **407**: 205-376 (2005)
21 V. Koch, T. S. Biro, J. Kunz, and U. Mosel, Phys. lett. B, **185**: 1 (1987)
22 I. N. Mishustin, L. M. Satarov, and W. Greiner, Phys. Rep., **391**: 363 (2004)
23 C. Da. Providencia, J. Da. Providencia, and S. A. Moszkowski, Int. J. Mod. Phys. B, **17**: 5208 (2003)
24 S. N. Wei, W. Z. Jiang, R. Y. Yang, and D. R. Zhang, Phys. Lett. B, **763**: 145-150 (2016)
25 T. J. Bürvenich and D. G. Madland, Nucl. Phys. A, **729**: 769 (2003)
26 H. Pais, D. P. Menezes, and C. Providencia, Phys. Rev. C, **93**: 065805 (2016)
27 S. Kubis, Phys. Rev. C, **70**: 065804 (2004)
28 S. Kubis, Phys. Rev. C, **76**: 025801 (2007)
29 X. D. Ji, Phys. Rev. Lett., **74**: 1071 (1995)
30 M. Procura, B. U. Musch, T. Wollenweber, T. R. Hemmert, and W. Weise, Phys. Rev. D, **73**: 114510 (2006)
31 W. G. Lynch, M. B. Tsang, Y. Zhang, P. Danielewicz, M. Famiano, Z. Li, and A. W. Steiner, Prog. Part. Nucl. Phys., **62**: 427 (2009)
32 C. Fuchs, Prog. Part. Nucl. Phys., **56**: 1 (2006)
33 I. Sagert, L. Tolos, D. Chatterjee, J. Schaffner-Bielich, and C. Sturm, Phys. Rev. C, **86**: 045802 (2012)
34 C. Fuchs, A. Faessler, E. Zabrodin, and Y. M. Zheng, Phys. Rev. Lett., **86**: 1974 (2001)
35 P. Danielewicz, R. Lacey, and W. G. Lynch, Science, **298**: 1592 (2002)
36 G. A. Lalazissis, J. Konig, and P. Ring,Phys. Rev. C, **55**: 540 (1997)
37 M. M. Sharma, M. A. Nagarajan, and P. Ring, Phys. Lett. B, **312**: 377 (1993)
38 Y. Sugahara and H. Toki, Nucl. Phys. A, **579**: 557 (1994)
39 B. A. Li and X. Han, Phys. Lett. B, **727**: 276 (2013)
40 L. W. Chen, C. M. Ko, B. A. Li, and J. Xu, Phys. Rev. C, **82**: 024321 (2010)
41 L. W. Chen, Nucl. Phys. Rev., **31**: 273 (2014)
42 C. Xu, B. A. Li, L. W. Chen, Phys. Rev. C, **82**: 054607 (2010)
43 M. B. Tsang, J. R. Stone, F. Camera, P. Danielewicz et al, Phys. Rev. C, **86**: 015803 (2012)
44 M. B. Tsang, Y. X. Zhang, P. Danielewicz, M. Famiano, Z. X. Li, W. G. Lynch, and A. W. Steiner, Phys. Rev. Lett., **102**: 122701 (2009); ibid., Int. J. Mod. Phys. E, **19**: 1631 (2010)
45 N. Wang, M. Liu, L. Ou, and Y. Zhang, Phys. Lett. B, **751**: 553 (2015)
46 J. M. Lattimer and Y. Lim, Astrophys. J., **771**: 51 (2013)
47 A. W. Steiner, S. Gandolfi, Phys. Rev. Lett., **108**: 081102 (2012)
48 X. Roca-Maza, M. Brenna, B. K. Agrawal, P. F. Bortignon, G. Col′ o, Li-Gang Cao, N. Paar, and D. Vretenar, Phys. Rev. C, **87**: 034301 (2013)
49 D. V. Shetty, S. J. Yennello, G. A. Souliotis, Phys. Rev. C, **76**: 024606 (2007)
50 P. Danielewicz and J. Lee, Nucl. Phys. A, **818**: 36 (2009)
51 M. Gearheart, W. G. Newton, J. Hooker, and B. A. Li, Mon. Not. R. Astron. Soc., **418**: 2343 (2011)
52 H. Sotani, K. Nakazato, K. Iida, and K. Oyamatsu, Mon. Not. R. Astron. Soc., **428**: L21 (2013)
53 W. G. Newton, B. A. Li, Phys. Rev. C, **80**: 065809 (2009)
54 J. M. Lattimer and A. W. Steiner, Eur. Phys. J. A, **50**: 40 (2014)
55 S. Gandolfi, J. Carlson, and Sanjay Reddy, Phys. Rev. C, **85**: 032801 (2012)
56 K. Hebeler, J. M. Lattimer, C. J. Pethick, and A. Schwenk, Astrophys. J, **773**: 11 (2013)
57 J. Oppenheimet and G. Volkoff, Phys. Rev., **55**: 374 (1939)
58 R. C. Tolman, Phys. Rev., **55**: 364 (1939)
59 G. Baym, C. Pethick, and P. Sutherland, Astrophys. J., **170**: 299 (1971)
60 K. Iida and K. Sato, Astrophys. J., **477**: 294 (1997)
61 P. Demorest, T. Pennucci, S. Ransom, M. Roberts, and J. Hessels, Nature, **467**: 1081 (2010)
62 J. Antoniadis, P. C. Freire, N. Wex, T. M. Tauris, R. S. Lynch et al, Science, **340**: 1233232 (2013)
63 A. W. Steiner, J. M. Lattimer, and E. F. Brown, Astrophys. J, **722**: 33 (2010)
64 A. W. Steiner, J. M. Lattimer, and E. F. Brown, Astrophys. J., **765**: L5 (2013)
65 S. Guillot, M. Servillat, N. A. Webb, and R. E. Rutledge, Astrophys. J, **772**: 7 (2013)
66 F. Özel, G. Baym, and T. Guver, Phys. Rev. D, **82**: 101301 (2010)
67 V. Suleimanov, J. Poutanen, M. Revnivtsev, and K. Werner, Astrophys. J, **742**: 122 (2011)
68 S. Bogdanov, Astrophys. J., **762**: 96 (2013)
69 J. Poutanen et al, Mon. Not. R. Astron. Soc., **442**: 3777 (2014)
70 C. O. Heinke, H. N. Cohn, P. M. Lugger, N. A. Webb et al, Mon. Not. R. Astron. Soc., **444**: 443 (2014)
71 J. M. Lattimer, A. W. Steiner, Astrophys. J., **784**: 123 (2014)
72 B. A. Li, A. W. Steiner, Phys. Lett. B, **642**: 436 (2006)
73 W. Z. Jiang, B. A. Li, L. W. Chen, Phys. Lett. B, **653**: 184 (2007)
74 G. Watanabe and C. J. Pethick, Phys. Rev. Lett., **119**: 062701 (2017)
75 J. M. Lattimer and M. Prakash. Phys. Rep., **333**: 121 (2000)
76 G. G. Pavlov, V. E. Zavlin, D. Sanwal, V. Burwitz, and G. P. Garmire, Astrophys. J., **552**: L129 (2001)